“BABEŞ-BOLYAI” UNIVERSITY CLUJ-NAPOCA

FACULTY OF PHYSICS

MEDICAL PHYSICS SPECIALIZATION

BACHELOR THESIS

THE INFLUENCE OF CHEMICAL INTERFACE DAMPING IN THE DEHALOGENATION OF 4-CLOROTHIOPHENOL AND 4-BROMOTHIOPHENOL ADSORBED ON SILVER NANOPARTICLES

Scientific coordinator

Prof. Dr. Nicolae Leopold

Graduate

Oana Maria Biro

2022

CONTENTS

INTRODUCTION 3

1. THEORY 6

1.1. PLASMONIC CHEMISTRY 6

1.1.1.LANDAU DAMPING 8

1.1.2.CHEMICAL INTERFACE DAMPING 9

1.2. SURFACE ENHANCED RAMAN SPECTROSCOPY 11

1.3. SINGLE PARTICLE DARK-FIELD SPECTROSCOPY 14

2. MATERIALS AND METHODS 17

2.1. SERS MEASUREMENTS 17

2.1.1.SYNTHESIS OF COLLOIDAL AGNPS 17

2.1.2.CSA SUBSTRATES 21

2.2. DFS MEASUREMENTS 24

2.2.1.MICROFLUIDIC SET-UP 24

3. RESULTS AND DISCUSSION 28

3.1. CID OF AGNPS WITH HALIDE IONS 28

3.2. CID OF AGNPS WITH CTP AND BTP 30

3.3. DEHALOGENATION OF CTP AND BTP TRACKED BY SERS 33

CONCLUSION 38

REFERENCES 39

Introduction

Chemical reactions dictate every process in our daily lives both from nature's standpoint as well as at an industrial level. In recent years, the scientific community has focused increasingly more on finding new, efficient photocatalysts – materials which can increase the chemical reaction rate under the influence of visible light. More specifically, the research focuses on increasing the chemical reaction efficiency and its cost-to-benefit ratio, thus allowing this process to be used industrially. The applications are vast, from improving photovoltaic cells to reducing air and water pollutants.

Recent studies have shown plasmonic photocatalysis as a new paradigm in the conversion cycle of solar energy to chemical energy. This process relies on plasmonic nanoparticles which can drive photoreactions, reduce activation barrier and unlock reaction pathways otherwise thermodynamically or kinetically impeded. [1] This type of metal nanoparticles is potentially useful in the development of many important technologies, such as molecular characterization, imaging, lasing and even cancer tissue targeting. [2]

Surface plasmon resonance (SPR) represents the coherent oscillation of free electrons in metal nanostructures, under the influence of radiative excitation. When light reaches the surface of a plasmonic nanoparticle, it excites collective oscillations of its conduction electrons. [1] This energy is then dissipated in two ways: radiatively through the emission of photons or through non-radiative decay, creating electron-hole pairs with energies higher than the thermal energy of bulk electrons (called hot-carriers) – a process called Landau damping. Their energy decays rapidly, in the order of tens of femtoseconds, due to multiple energy dissipation pathways, bulk damping, radiation damping, surface scattering and chemical interface damping (CID). [3] In the space of picoseconds, the relaxation of a plasmonic mode in a nanocrystal consists of electron-electron scatterings, electron-phonon scatterings, finally dissipating heat into the environment, as shown in Figure 0.1.

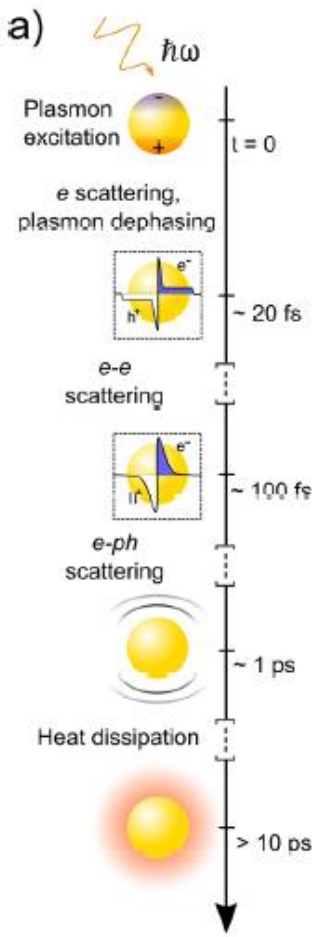

Figure 0.1 Schematic of the time scales of the steps involved in the relaxation of a plasmonic mode [4]

In order to master the applications of plasmonic photocatalysis it is of the utmost importance that we understand the mechanism of charge transfer from the nanoparticles to adsorbed molecules. Chemical interface damping represents the direct charge transfer from the plasmon resonance to molecular orbitals close to the nanoparticles' Fermi level, which can be experimentally observed by tracking the plasmon resonance decay in frequency space – the halfwidth of the plasmonic band.

As such, the goal of this thesis is to monitor the influence of the formation of nanoparticle-adsorbate systems in the plasmon resonance decay and consequently in driving a chemical reaction. In order to observe such complex effects, we track the dehalogenation of 4-bromothiophenol (BTP) and 4-clorothiophenol (CTP) under the influence of plasmon resonance energy transfer from silver nanoparticles (AgNPs) using surface enhanced Raman spectroscopy (SERS) and single particle dark field spectroscopy (DFS).

Gaining a deeper insight into the mechanisms of chemical interface damping and its influence in driving chemical reactions is an important step towards developing CID based biosensors which can detect real biological molecules that contain thiol groups. [11]

The first chapter introduces the theory on which this thesis is based upon. Two mechanisms of charge transfer – Landau damping and chemical interface damping – are presented in detail as well as the theoretical background for SERS and DSF.

The second chapter describes the methods used during this research. It contains an account of the synthesis of the colloidal silver nanoparticles as well as the subsequent substrate formation through convective self-assembly (CSA) and the procedure used for SERS measurements. Afterwards, the microfluidic set-up is presented, as well as the procedures for the DFS measurements.

The third chapter presents the results of these measurements and their analysis. Finally, a conclusion is formulated based on these results.

1. Theory

1.1. Plasmonic chemistry

Plasmonic chemistry studies the interaction between plasmonic nanoparticles and their environment – specifically how chemical reactions can be triggered by the decay of plasmon energy through multiple dissipation pathways.

Before delving into the theory for damping pathways, we must first have a basic understanding of plasmonic nanoparticles and the phenomena that surrounds them. When light falls directly on a metal nanoparticle, its negative charges accumulate on one of its sides, pushed by the particle's electric field, thus leaving a positive charge on the other side of the particle. These two sides attract one another and if the negative charge would suddenly be released, then it would oscillate with a certain frequency – much like a mass on a spring, which is why we can think of this system as a damped harmonic oscillator. If the frequency of the incident light matches this natural resonance frequency, all the free electrons in the metal would oscillate together and create large electric fields in the vicinity of the particle. The produced fields act on the electrons as well, reinforcing the oscillation. Plasmon resonance (or particle plasmon) consists of this coupled excitation – the oscillating charges inside the particle and the oscillating electromagnetic fields immediately adjacent to the particle. [6]

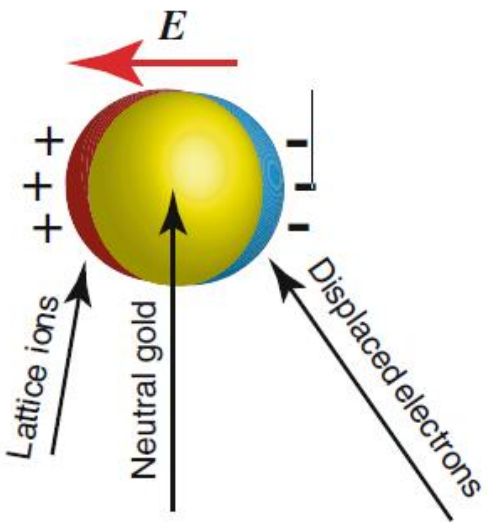

Figure 1.1. Schematic of charge separation [5]

Considering this, we can think of metals as positively charged atomic nuclei surrounded by a plasma of free electrons from the conduction band and therefore surface plasmon resonance is the collective oscillation of plasma near the nanoparticle's surface when it is irradiated. [8]

Plasmon relaxation can trigger chemical reactions in its environment by transferring energy to molecules adsorbed on its surface. The result is the possibility of selective photocatalysis through the use of nanoparticles - chemically transforming target molecules in a mixture containing multiple substances. In order to control this, we must first understand the theoretical background of plasmon damping.

There are several energy dissipation pathways of the plasmon resonance modes, the main ones being:

- Radiative damping – in which the energy is dissipated through the emission of electromagnetic radiation;
- Surface scattering – the dissipated plasmonic resonance energy goes towards creating electron-hole pairs with higher energy than that of the metal electrons. These hot charge carriers can reach the surface of the plasmon and scatter, a process called Landau Damping;
- Bulk damping – electron-electron and electron-phonon scattering which dissipate the energy through thermal heating;
- Chemical Interface Damping – in which there is a direct energy transfer from the plasmon to an adsorbed molecule.

In the context of plasmonic chemistry, we must observe the mechanism of charge transfers from the plasmon to surrounding molecules – Landau Damping (indirect energy transfer) and Chemical Interface Damping (direct energy transfer).

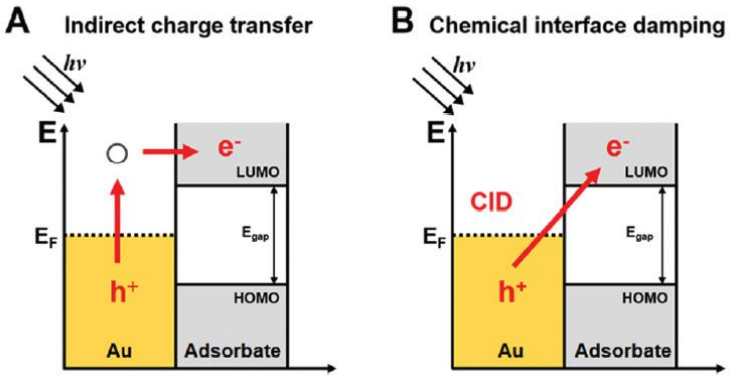

Figure 1.2. Schematic representation of direct and indirect charge transfer in gold nanoparticles (A) Indirect transfer with the intermediate step of electron-hole pair formation in the nanoparticle (B) Direct transfer through the generation of hot electrons directly in the adsorbate's LUMOs. [11]

1.1.1. Landau Damping

After the interaction of light with the nanoparticle, the plasmon relaxes by forming high energy electron-hole pairs, a process that lasts a few femtoseconds. These hot charge carriers then collide with electrons or phonons, dissipating thermal energy and heating the nanoparticle. The entire thermalization lasts a few hundred femtoseconds.

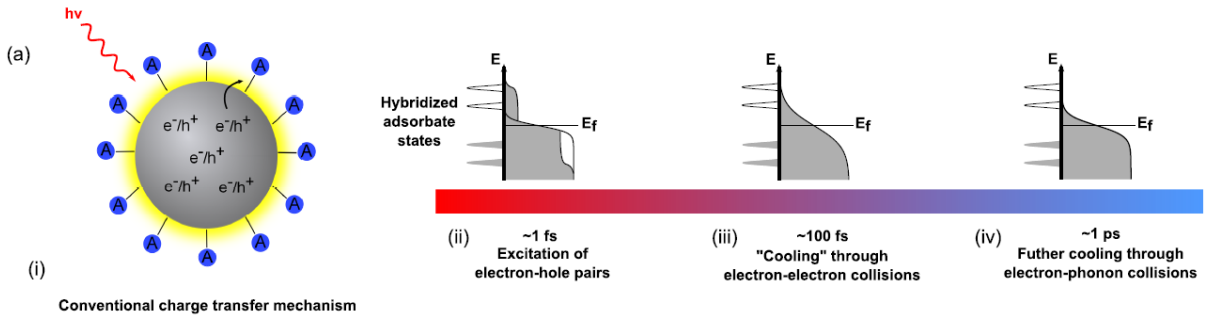

Figure 1.3. Schematic representation of Landau Damping (i) photon interaction with the nanoparticle. (ii) the electron-hole pairs form an athermal distribution. (iii) the hot electrons scatter through collision with other electrons. (iv) the hot electrons collide with phonons [9]

Landau Damping refers to the surface scattering of these hot electrons. The electron-hole pairs can potentially reach the surface of the plasmon and escape the metal through tunneling, transferring charge to an adsorbed molecule. This process can happen anytime during the cooling down period and is entirely probabilistic. However, the yield of

extracted electrons is low because of the small timeframe and the fact that there are only few electron-hole pairs with energy high enough to be transferred.

Landau Damping is dependent on hot carrier generation, which in turn is proportional to the electric field intensity. [22] The enhanced electric field can improve light harvesting, thus generating more hot electrons which can be transferred to the adsorbed molecule, driving a chemical reaction. [23]

In order to quantify Landau Damping we can take a look at the reaction rate which can be extracted from SERS spectra. Due to the inhomogeneity of the substrate, studies show that a fractal reaction constant better describes the kinetics of the reaction, resulting in the following equation [22] :

$$I = I_0 \cdot \frac{e^{k \cdot t^{(1-h)}}}{(1-h)} \tag{1}$$

Where I is the SERS signal intensity, I_0 is the incident light intensity, k is the fractal reaction constant and h is the degree of inhomogeneity of the substrate.

1.1.2. Chemical Interface Damping

Compared to Landau Damping, Chemical Interface Damping skips the step of hot electron creation, meaning the energy is transferred directly to the adsorbate. This proposed mechanism is rather new and less understood than the conventional one, but it has the highest contribution to charge transfer. It has been attributed to a number of mechanisms which accelerate the plasmon decay: charge transfer, dipole scattering and resonance energy transfer. [10]

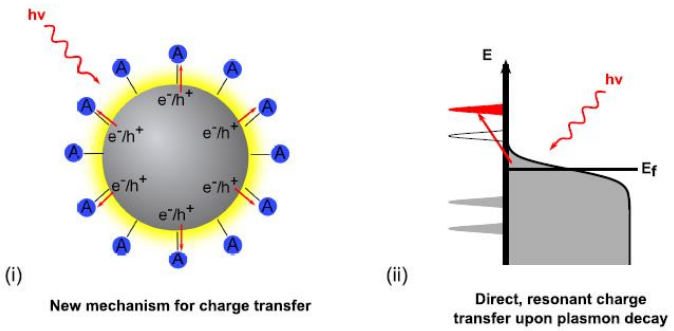

Figure 1.4. Schematic representation of Chemical Interface Damping [9]

Through this dissipation channel, the hot electrons are directly transferred to empty LUMOs (lowest unoccupied molecular orbitals) of the adsorbate. This process leads to a proportional change in the localized surface plasmon resonance (LSPR) linewidth, position and intensity and therefore it can be monitored.

Because the dephasing process happens in a matter of femtoseconds, it cannot be properly measured in time-domain, but since time and frequency are linked by the Fourier transformation, the dephasing times can be studied in frequency-domain by analyzing the spectral broadening of the oscillating system.

If we consider an oscillating electric field E(t), with an eigenfrequency ω_0 whose oscillation decays exponentially with a time constant T, the Fourier transformation implies that the frequency spectrum obeys a Lorentz-line shape:

$$E(t) = (E_0 e^{-i\omega_0 t})e^{-t/T} \tag{2}$$

$$E'(\omega) = \mathcal{F}\big(E(t)\big) = \frac{E_0}{\sqrt{2\pi}} \frac{1/T}{(\omega - \omega_0)^2 + (1/T)^2} \tag{3}$$

Considering the fact that a Lorentz line is characterized by its center position ω_0 and full width at half maximum (FWHM) $\Delta\omega$, we can convert the FWHM to a decay time using the following formula:

$$\frac{T}{fs} = \frac{1316}{\Gamma/meV} \tag{4}$$

Where $\Gamma = \hbar\Delta\omega$. [24]

We can use Person's theory to estimate the chemical interface damping from the plasmon dephasing rate through the following formula:

$$\gamma = \gamma_0 + C\frac{v_F}{r} \tag{5}$$

Where γ_0 is the bulk damping rate of silver, v_F is the Fermi velocity and r is the radius of the nanoparticles. The C factor describes the rate of the energy transfer from the plasmon to the adsorbate, and therefore can be used to quantify the chemical interface damping.

1.2. Surface-Enhanced Raman scattering

Raman Spectroscopy deals with the study of inelastic light scattering that provides information about a molecule's vibrational structure. Surface enhanced Raman spectroscopy (SERS) is a technique used to amplify by several orders of magnitude the Raman signal by using plasmon resonance.

Spectroscopy is a field that studies the interaction of light with matter, which can be absorbed or scattered. While infrared spectroscopy deals with the absorption of light by molecules, Raman spectroscopy is based on the scattering of light. They are complementary techniques (for example symmetrical stretch vibrations can't be observed in IR spectra but the appear in Raman vibrational spectra).

When a molecule is irradiated with light, it can be excited to a virtual electronic state (a state between the ground state and the lowest electronic state). Because it is not a real state, but a virtual one, the electron will quickly (a few nanoseconds) return to the ground state (i.e., get scattered). There are now three options:

- Rayleigh scattering – where the electron returns to the same state it originated from, the energy of the scattered photon being the same as the incident one.
- Stokes scattering – where the electron returns to a higher vibrational state than the one it originated from, the energy of the scattered photon being lower than the incident one.
- anti-Stokes scattering – where the electron returns to a lower vibrational state than the one it originated from, the energy of the scattered photon being higher than the incident one.

The loss in energy between the incident photons and the scattered photons is called Raman shift and is defined as $\Delta E_R = E_L - E_S$ and it is positive for a Stokes process and negative for an anti-Stokes one. It is usually expressed in wave numbers, denoted as $\Delta\bar{\nu}_R$ and measured in $[cm^{-1}]$. Its modulus equals to the wave number of the vibrational mode that was involved in the scattering event. The Raman spectrum is displayed as Raman intensity as function of Raman shift, as shown in Figure 2.5. [12]

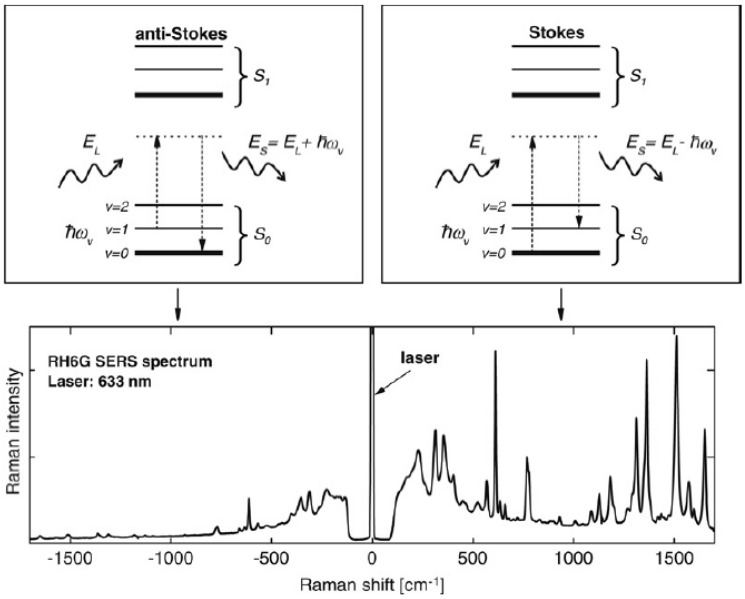

Figure 1.5 The top images depict the Stokes and anti-Stokes processes using simplified Jablonski diagrams, while the lower image shows a typical SERS spectrum for rhodamine 6G. The peak at $\Delta\bar{\nu}_R = 0$ corresponds to the Rayleigh scattering, respectively the laser line [12]

Despite its usefulness as an analytical tool, Raman spectroscopy has not been used at its full potential for many years due to its inefficiency. The typical Raman scattering cross-section is only circa $10^{-29} cm^2/molecule,$ [8] while that of fluorescence is circa $10^{-16} cm^2/molecule$. The cross section measures the extent of photon-molecule interactions, so the larger the cross section, the stronger the interaction which translates to a stronger signal and higher sensitivity. [12]

Surface enhanced Raman scattering amplifies the Raman signal by several orders of magnitude, increasing the sensitivity to one that is often comparable to that of fluorescence. The enhancement is attributed to the amplification of the local electromagnetic fields related to the excitation of surface-plasmon resonance. [13] To profit from this enhancement, the molecules must be adsorbed on a metallic surface (or be very close to it). These metallic surfaces are represented by metallic nanostructures

such as metallic colloids in solution or substrates fabricated by nano-lithography or convective self-assembly.

The SERS effect has been first observed in 1974 by Fleischman et al. who reported a significant amplification of the Raman signal measured for pyridine absorbed on an electrochemically nanostructured silver substrate. They interpreted this phenomenon as being attributed to the increased surface area of the electrochemically roughened silver electrode, which resulted in the adsorption of a larger number of pyridine molecules. In 1977, two different research groups have discovered the real reasons behind this amplification. Jeanmarie and van Duyne, and Albrecht and Creighton noticed the connection between the increased efficiency of Raman scattering and the strong Raman signal observed for pyridine adsorbed on the nanostructured silver surface and the effect was named SERS. [8]

The SERS intensity is proportional to both the laser intensity and the normal Raman cross section of the molecule and it is amplified by an enhancement factor (EF). This enhancement is mainly due to electromagnetic enhancement but there is also a small contribution attributed to chemical enhancement.

To better understand the electromagnetic enhancement, Kerker et al used a model consisting in a molecule adsorbed at the surface of a spherical particle and treated it as a classical electrical dipole. The molecule is excited by a primary field comprised of the incident and near-scattered fields, while the emission consists of the dipole field and a scattered field, both at a shifted frequency. [14] The Raman scattering observed in this system will have two components: an induced oscillating dipole p_1, with the Raman frequency ω and a dipole induced by a scattered field p_2 with the shifted Raman frequency ω. In the radiation zone, the detected Raman field for this system will have contributions from the electric field created by p_1 coherently added with the field given by p_2. The total power is proportional to the square of their sum. In order to evaluate the enhancement factor, we need to compare it to the power of the molecule p_M in absence of the metallic sphere. [15]

$$EF = \frac{|p_1 + p_2|^2}{|p_M|^2} \tag{6}$$

This enhancement factor does not include the chemical enhancement that can arise from the metal-molecule proximity, but its contribution is small to the overall enhancement.

This effect requires the molecules to be chemically adsorbed on the surface of the metal, thus forming a complex which modifies the Raman polarizability tensor of the adsorbate through a charge transfer mechanism. There are three types of charge transfers [12]:

1. If the adsorbate does not covalently bind to the metal, the metal acts as a perturbation to the electronic structure of the analyte, determining a small change in its electronic distribution and its polarizability.
2. If the metal and molecule form a surface complex through covalent binding or by use of an electrolyte ion, this will produce a substantial change in the polarizability of the molecule.
3. If the difference between the Fermi level of the metal and the HOMO or LUMO energies is matched by the laser, there can be a photo-driven charge transfer.

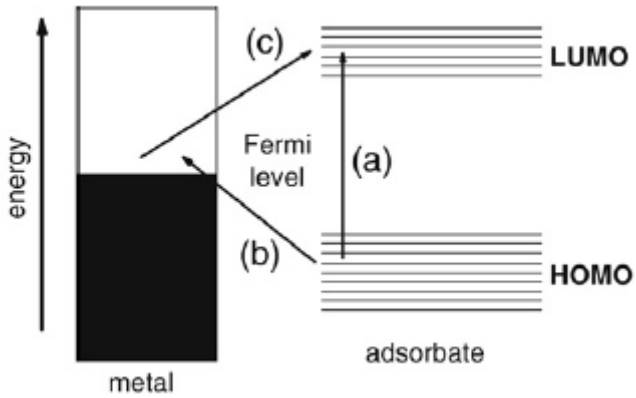

Figure 1.6. Schematic representation of charge transfer mechanisms. (a) represents the photo-driven charge transfer, while (b)+(c) represent a classical indirect charge transfer [12]

In conclusion, Surface enhanced Raman scattering provides a great improvement in the sensitivity or Raman signals both through electromagnetic enhancement as well as chemical enhancement.

1.3. Single Particle Dark-Field Spectroscopy

The conventional method of acquiring microscopic images is through bright-field illumination, where light from the illumination source covers the entire field of view and the image is made up from the light that is either transmitted or reflected by the sample.

Dark-field microscopy uses a special condenser that blocks the light from the center of the beam so that the light is incident on the sample at high angles. The light is then collected by an objective lens with a numerical aperture small enough that it does not collect the high-angle illumination directly transmitted by the sample. Only the light that is scattered at lower angles will enter the objective and form the image, thus creating bright spots on dark backgrounds. This method is very useful for samples whose scattering would be too faint to see in bright-field illumination, but can be easily seen in a dark-field image – just as we cannot see the stars during the day because of the sunlight. [6]

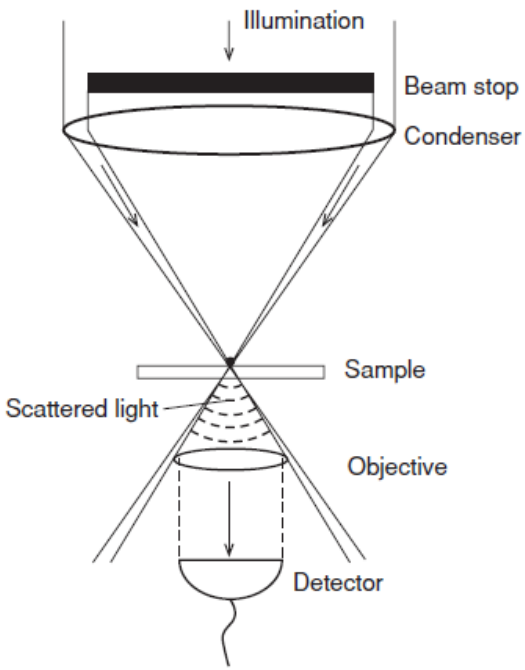

Figure 1.7. Schematic representation of dark-field microscopy [6]

Dark-field microscopy provides a high contrast suitable for low-contrast objects with refractive indexes similar to the background. Because it focuses only on reflected light from the sample, it successfully eliminates background noise.

Hyperspectral imagery (HSI) is a technique in which besides acquiring 2D intensity images, there is another dimension in the form of spectra, resulting in a three-dimensional datacube. In simpler terms, there is a spectrum acquired for each pixel, the hyperdata cube containing both spectral and spatial information. The method is sensitive to subtle spectral changes, thus easily discriminating between analytes. [16]

The combination between dark-field microscopy and hyperspectral imaging is ideal for optically studying nanoparticles. Dark-field illumination generates images with high contrast and enhanced signal-to-noise ratio, while the spectrometer is able to measure the spectral signature for each pixel thus offering complex information about the studied nanomaterials.

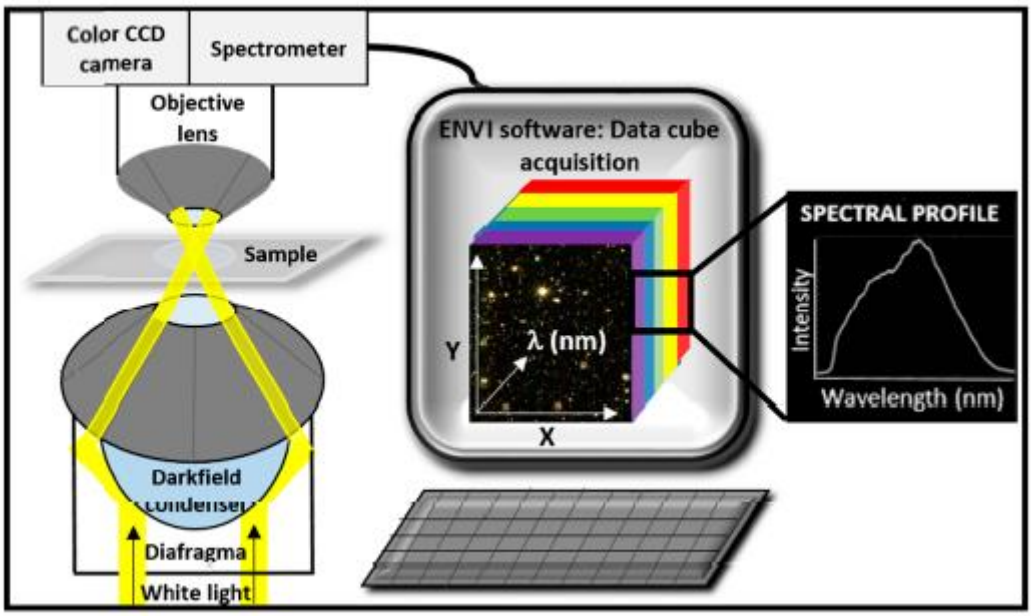

Figure 1.8 Schematic representation of a hyperspectral enhanced dark field microscopy system [16]

For silver nanoparticles, the spectrum is dominated by the localized surface plasmon resonance (LSPR) whose linewidth is proportional to the plasmon damping rate. The LSPR linewidth depends on particle size, shape and environment. Therefore, because samples of metal nanoparticles are generally heterogenous – different sizes and shapes, we must concentrate on studying single particles and not the ensemble as a whole. [17]

Single particle spectroscopy can be effectively used to study plasmon damping pathways. [11] Certain adsorbed molecules induce a broadening of the LSPR linewidth, which can be measured using hyperspectral enhanced dark field microscopy.

2. Materials and methods

2.1. SERS measurements

For accurate SERS measurements we required monolayered substrates of monodisperse silver nanoparticles. In order to achieve that, we have first synthesized appropriate AgNPs and then we have constructed a convective self-assembly (CSA) setup that produces reproductible substrates in the form of nanowires.

After the synthesis of the substrates, they were placed under the microscope, where BTP and CTP were added by pipetting, several minutes being allowed for the substances to adsorb to the substrate. Several 60 s time-series measurements were performed, using both the 532 nm laser line at 0.5% and 1% power and the 633 nm laser line at 5% and 10% power.

After the measurements were taken, they were analyzed using a Matlab script to extract the peaks corresponding to the dehalogenation reaction. The bands at 1066 cm^{-1} and 1061 cm^{-1}, corresponding to the C-Br and C-Cl vibrations decrease as time goes on following the (2.1) equation described in the theoretical chapter.

By fitting the measurements in Excel using that formula, we can extract the fractal reaction rate k and compare it between the two substances.

2.1.1. Synthesis of colloidal AgNPs

A vast majority of the existent plasmonics research is centered on gold and silver nanoparticles because they have plasmonic resonance in the visible electromagnetic range. They also have a high density of conduction electrons: more electrons are involved in a plasmon oscillation resulting in a greater electrostatic restoring force and thus a greater resonance frequency. Moreover, the losses are relatively low in these two metals compared to others, such as copper which can support plasmonic resonances at optical frequencies but they are weak because the plasmons are quickly dissipated due to losses. We have based our research on silver nanoparticles because it has the lowest losses and therefore the strongest plasmon resonances of all known materials. [6]

Besides the material they are made of, another important characteristic of metal nanoparticles is their shape. The electric fields around the particles depend on their shape, sharp points and high aspect ratios concentrate the fields which results in lower restoring forces and therefore lower resonance frequencies. [6]

Through modifying the classic Lee-Meisel synthesis method [7] we have managed to obtain monodisperse silver nanoparticles. Through the chemical reduction of $AgNO_3$, we have obtained monodisperse spherical silver nanoparticles with a diameter of approximately 80 nm. The method is based on the reduction of $AgNO_3$ by a sodium citrate in a water solvent.

17 mg of $AgNO_3$ were added to 100 ml of H_2O and brought to a boil, after which 2 ml of 1% sodium citrate solution were added to the mix. The resulting solution was kept boiling for half an hour, time in which the silver atoms nucleated together, forming nanoparticles. As this process went on, the solution became more and more opaque as the particles grew in size.

To make sure our synthesis was successful, we have conducted a visual analysis using transmission electron microscopy (TEM). The resulting image can be seen in the following figure.

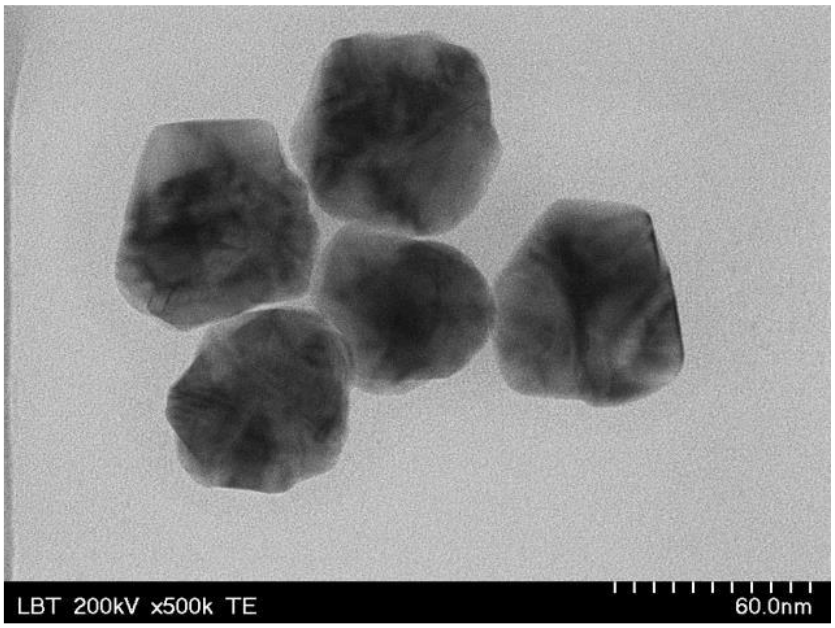

Figure 2.1. TEM image of the synthesized AgNPs

TEM images were analyzed using the ImageJ software to assess the diameter of the nanoparticles, as shown in the table in Figure 3.2, resulting in a mean diameter of 59.696 nanometers.

	Label	Area	Mean	Min	Max	Angle	Length
1		24.972	60.132	22.176	156.000	-91.872	61.644
2		25.296	60.164	31.097	171.000	-93.691	62.546
3		24.972	66.740	34.320	155.359	-82.875	61.684
4		22.864	59.822	30.100	195.188	-94.934	56.181
5		22.864	58.766	25.564	123.000	-47.314	56.425
6	Mean	24.194	61.125	28.652	160.109	-82.137	59.696
7	SD	1.221	3.190	4.787	26.295	20.033	3.119
8	Min	22.864	58.766	22.176	123.000	-94.934	56.181
9	Max	25.296	66.740	34.320	195.188	-47.314	62.546

Figure 2.2. ImageJ measurements of the nanoparticles' diameters, based on the TEM image

We have also performed a more detailed and precise analysis using NanoSight NS300 which uses nanoparticle tracking analysis (NTA) for nanoparticle characterization. It provided information about the size distribution as well as the concentration of the AgNPs, as shown in Figures 3.3, 3.4 and 3.5.

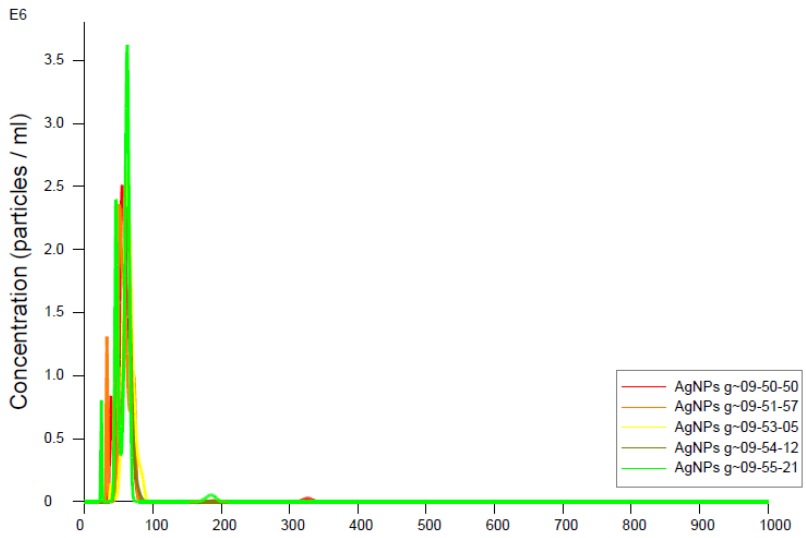

Figure 2.3 Nanoparticle size distribution as a function of concentration

Nanoparticle tracking analysis measures the particles' size by video tracking their Brownian motion in a number of frames, their movement being dependent on how big or small they are. Their concentration is measured by observing the number of particles in one frame and then calculating the average count one particle is observed in different frames divided by the volume interrogated. This type of measurement is shown in the figure above.

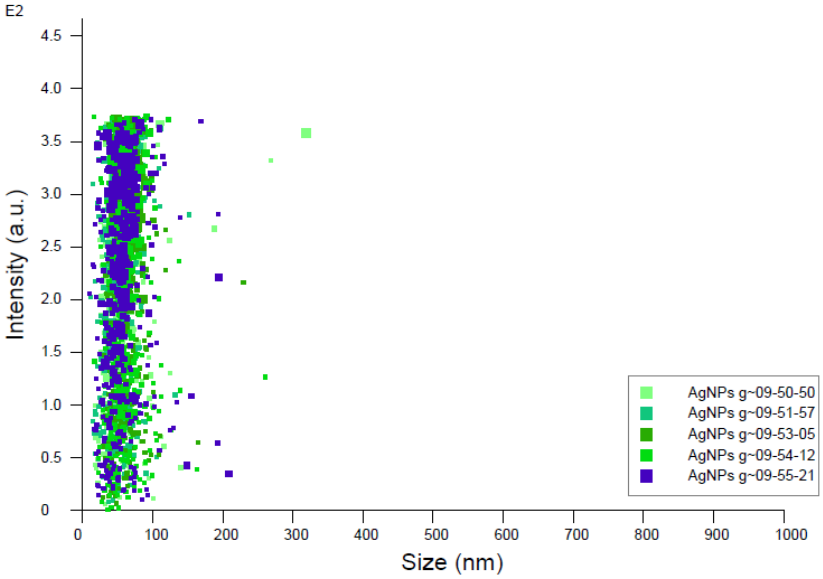

Figure 2.4 Nanoparticle size distribution as a function of scattering intensity

NTA is also able to register the amount of light scattered by each particle and plot it against its size, which is shown in Figure 3.4.

Results

Stats: Merged Data

Mean:	59.6 nm
Mode:	61.9 nm
SD:	18.0 nm
D10:	45.4 nm
D50:	58.7 nm
D90:	68.7 nm

Stats: Mean +/- Standard Error

Mean:	59.7 +/- 1.3 nm
Mode:	58.7 +/- 2.4 nm
SD:	15.7 +/- 4.0 nm
D10:	46.4 +/- 2.1 nm
D50:	58.4 +/- 1.4 nm
D90:	68.5 +/- 1.5 nm
Concentration (Upgrade):	4.16e+007 +/- 1.15e+006 particles/ml
	7.1 +/- 0.2 particles/frame
	8.0 +/- 0.2 centres/frame

Figure 2.5. Summarized results of NTA measurement

This analysis has confirmed that we have synthesized nanoparticles with a mean diameter of 59.6 nm with a standard deviation of 18 nm.

Another useful information is the concentration of the colloid, which from the analysis is 4.16×10^7 nanoparticles/ml. We have diluted our colloid 1000 times, therefore the real concentration of particles was 4.16×10^4 nanoparticles/ml.

2.1.2. CSA substrates

If a colloid is left to dry on its own on a microscope slide, it would form nanoparticle agglomerations which would hinder measurements. In order to obtain proper results, monolayered substrates need to be created. Convective deposition is a scalable method that is used to direct colloidal self-assembly. [18] The general set-up implies two glass slides positioned at a 30° angle, in between which there is a drop of colloidal suspension. By translating one of the slides, the meniscus is dragged into a thin film and the nanoparticles form ordered structures at the substrate-liquid-air contact line due to solvent evaporation. [19] By controlling the relative movement of the slides in a stop-and-go fashion we managed to assemble the nanoparticles into an ordered array of wires.

Figure 2.6. A schematic representation of the stop-and-go CSA method

The set-up was constructed in a do-it-yourself manner. First, a precise motorized translation stage was picked out: ThorLabs KMTS50 E/M whose maximum displacement is 50 mm at a minimum speed of 50 µm/s. Although the actuators conventionally used in literature moved at a speed of 20-25 µm/s, we have obtained satisfactory results with this higher speed.

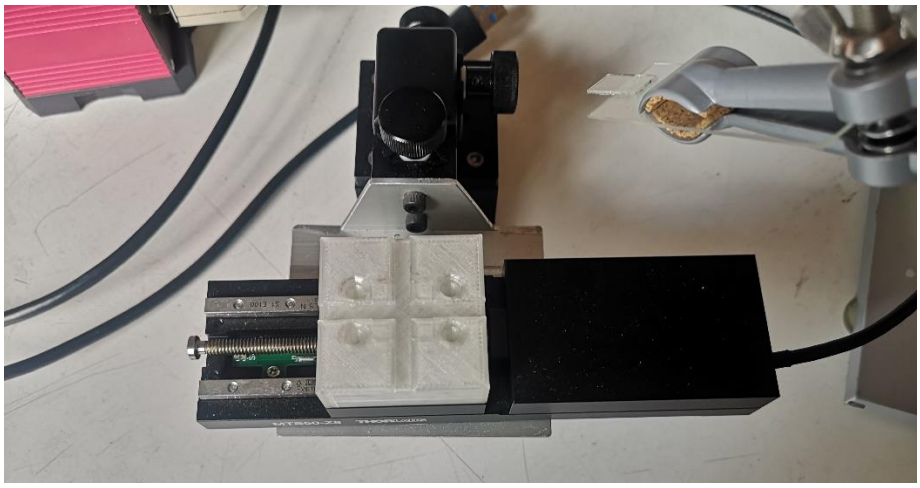

Figure 2.7. Top view of the actuator equipped with the slide support system

The linear actuator is used to hold the horizontal slide and translate it. In order to secure the fixed slide to the translating stage, a support was designed and 3D printed. It can hold a 15 x 15 mm glass slide, which is enough for the needed substrates.

The next step was to create a support system for the actuator and the fixed glass slide, which we have assembled with various supports found in the University's laboratories, as can be seen in Figure 3.8.

Figure 2.8 Lateral view of the CSA set-up

The actuator was controlled using the Kinesis software provided by ThorLabs. It allowed us to create the sequence shown in Figure 3.9, in which the stage moves at the lowest

speed a certain number of steps, it stops for 5 seconds and then it repeats these two steps. The entire sequence is repeated a number of times, so that the entire slide is covered in wires.

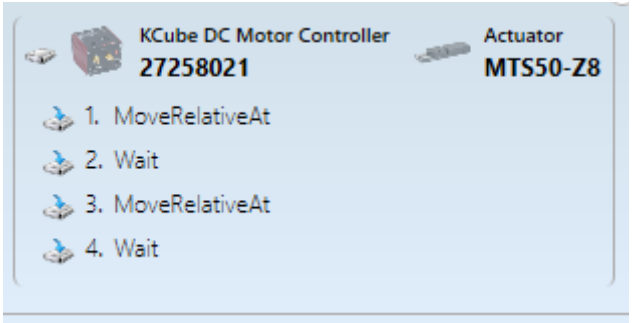

Figure 2.9. The command sequence for the linear actuator

We were able to obtain wires spaced at 100, 250 and 500 µm, with a reproductible wire width of 10 µm. Figure 3.10 shows images of each of these substrates obtained with the Leica microscope equipped on the Raman spectrometer we used for measurements.

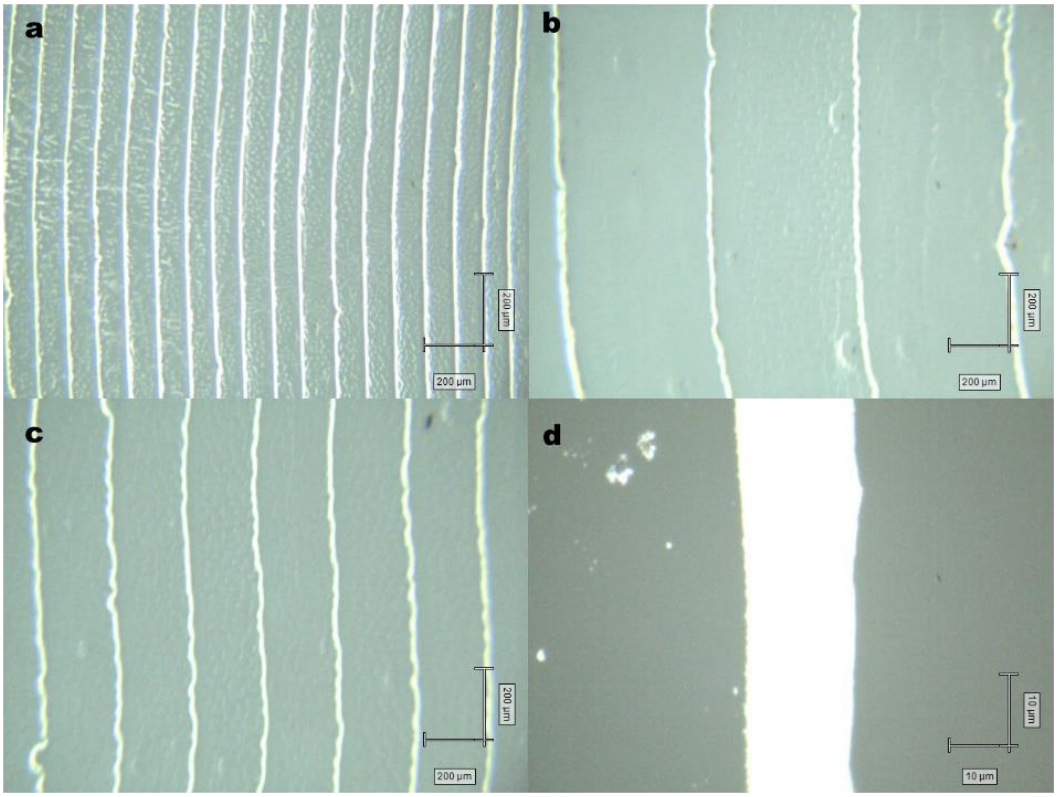

Figure 2.10. a. Nanowires spaced at 100 µm apart; b. Nanowires spaced at 500 µm apart; c. Nanowires spaced at 250 µm apart; d. Close-up image of a nanowire with a 10 µm width.

The SERS spectra were acquired on an InVia Raman Spectrometer coupled with an upright Leica microscope. Two laser lines were used: 532 nm and 633 nm. To focus the laser on the sample, a x5 microscope objective was used. The laser power was measured beforehand, resulting in the following table.

Laser line [nm]	633		532			785	
Power percentage [%]	10	100	1	5	10	1	10
Power [mW]	0.55	6.20	0.60	3	4.90	0.70	6.40

Table 2.1. Laser power

2.2. DFS measurements

2.2.1. Microfluidic set-up

To observe the changes in the localized surface plasmon resonance (LSPR) linewidth, we have taken dark field scattering measurements using a Cytoviva Hyperspectral Dark Field Microscope. The spectral data was acquired using light in the visible range, using a x40 microscope objective. The colloid was dried off inside a microfluidic cell, which allowed the different substances to be circulated through to properly measure the changes.

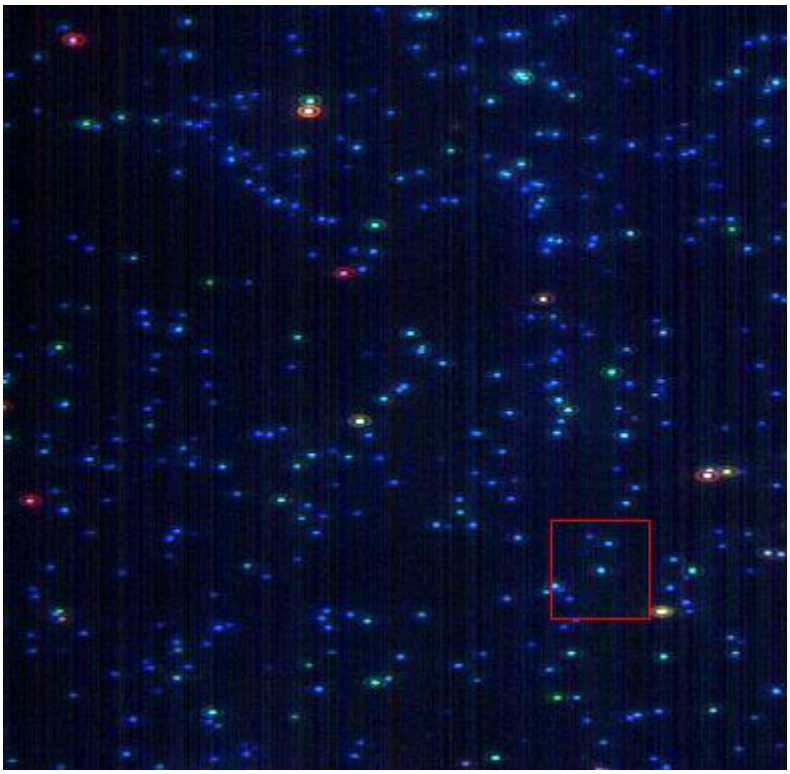

Figure 2.11. Dark Field Scattering image of AgNPs@ethanol

In order to circulate the substances through the microfluidic cell, a microfluidic pump was required. We have designed one, 3D printed its components and assembled it in the laboratory. The basic principle on which the project relies is the constant push of a syringe through a slow and controlled movement. We have achieved that by mounting the syringe barrel on a support, while the syringe plunger was fixed to a moving carriage. The movement of the carriage was achieved through a nut-screw mechanism, a nut being fixed inside the carriage with a stepper motor rotated screw passing through it. With each turn of the screw, the carriage moved an increment forward, pushing the syringe plunger which in turn pushed the substance through a tube and into the microfluidic cell.

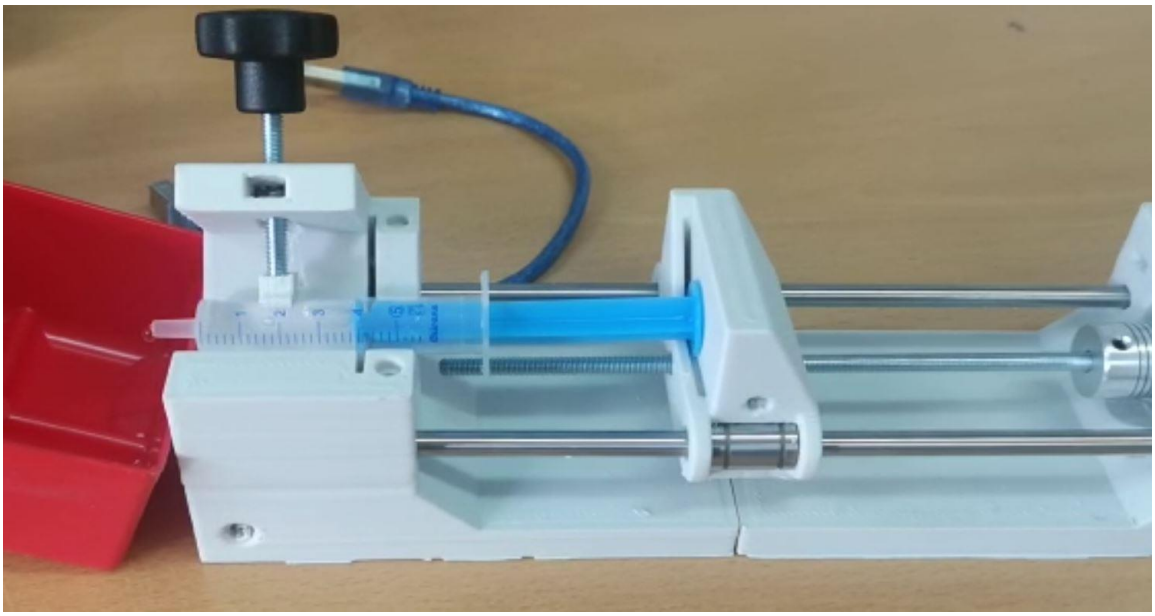

Figure 2.12. Lateral view of the microfluidic pump

The microfluidic pump was controlled through G-code, the same machine language that is used for CNC routers or 3D printers. After each substance was passed through the cell, the carriage would be moved backward to its “home” position by rotating the stepper motor in the opposite direction.

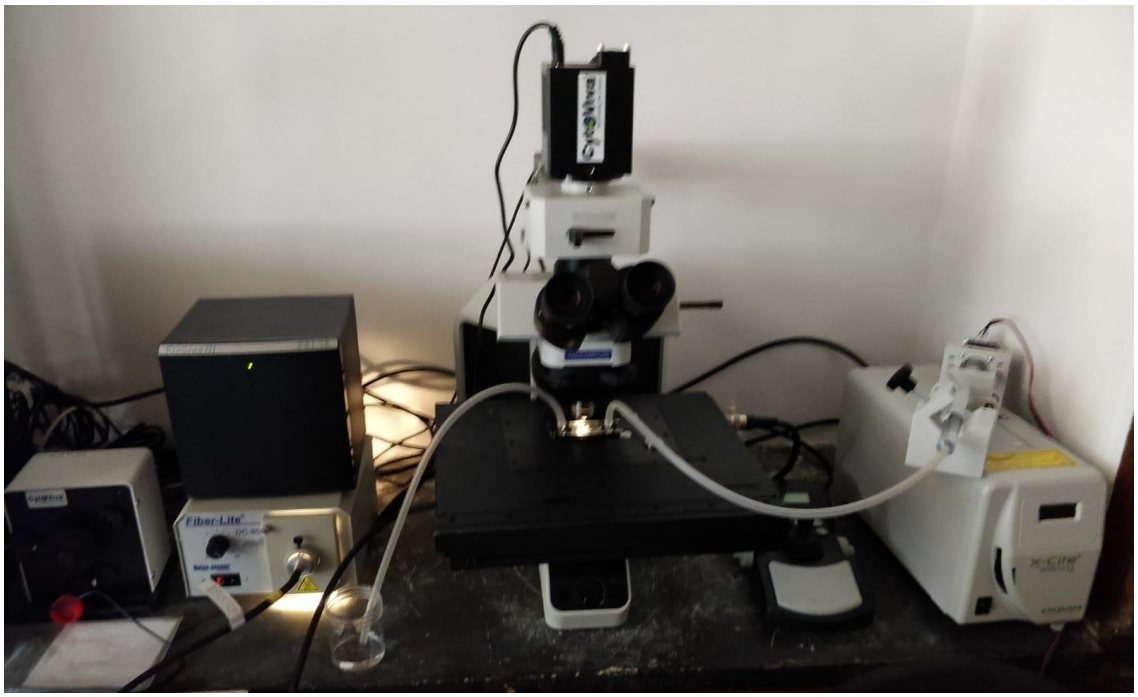

Figure 2.13. DFS experimental set-up

There were two measurements taken each time so CID could be observed: an image of the sample in ethanol and an image of the sample in either CTP or BTP. Both 4-Chlorotiophenol (CTP) and 4-Bromotiophenol (BTP) were dilluted 1:9 with ethanol.

For each measurement, the microscope was focused on the sample and then a proper measurement zone was searched (one that had as few nanoparticle agglomerations as possible, so that single-particle measurements can be taken). After the measurements were acquired, the image was enhanced using a linear filter and normalized to the lamp spectrum. In order to take the measurements at a single-particle level, 20 nanoparticles were chosen in the ethanol image such that their spectrum resembled a Lorentzian curve, their coordinates taken down, their spectral profiles saved and then the same 20 nanoparticles would be investigated in the CTP (BTP) image, their spectral profiles saved as well.

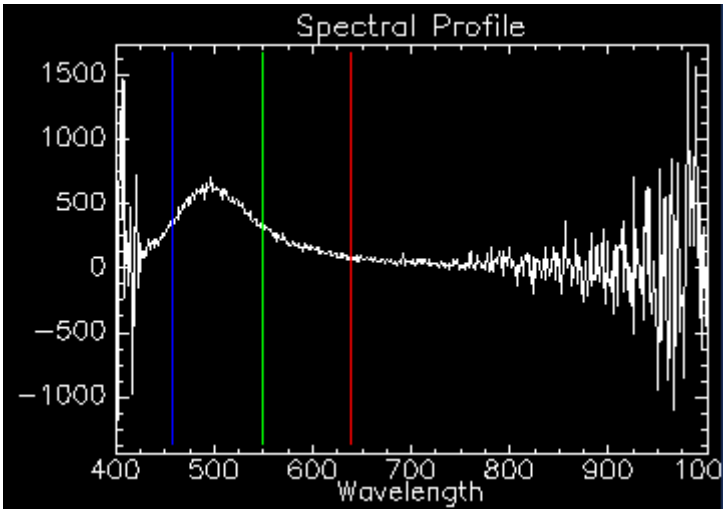

Figure 2.14 Spectral profile of AgNP@BTP

3. Results and discussion

3.1. CID of AgNPs with halide ions

At the beginning of our study, we created a test system consisting of halide ions and AgNPs, in which we quantified the interaction between the nanoparticles and the adsorbed molecules, the results being published in ACS Photonics at the begging of the year. First, we synthesized spherical silver nanoparticles with a diameter of approximately 100 nm for which we have measured their surface plasmon resonance (SPR) using the dark field scattering set-up previously presented. After the colloidal solution of AgNPs was deposited and dried in a microfluidic cell, we used the microfluidic pump to sequentially add ultrapure water, NaCl, KBr and KI (1 mM) taking a spectra measurement after each solution was pumped through. The spectra were then fitted with a Lorentzian curve, as shown in the following figure.

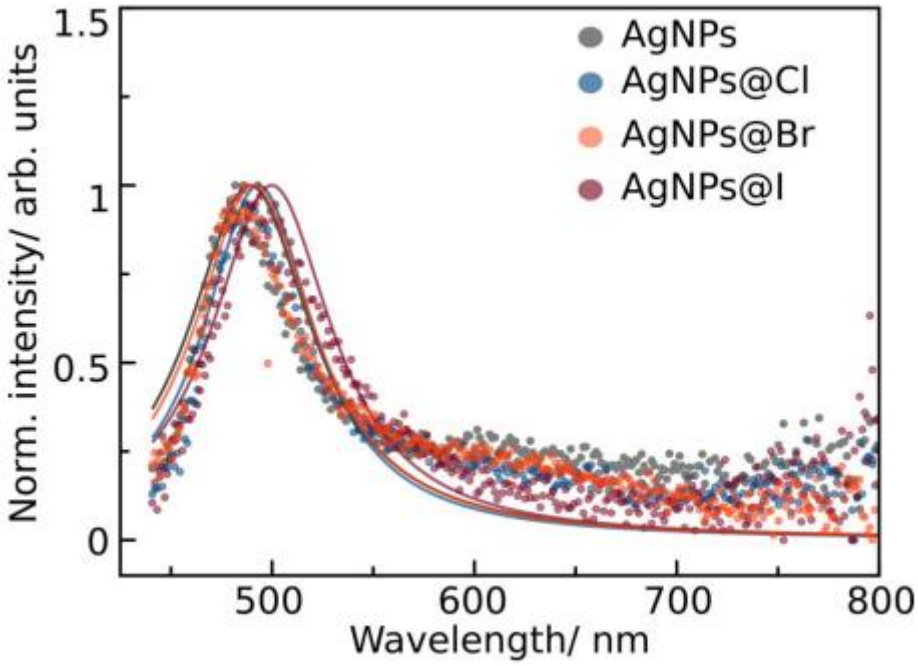

Figure 3.1. The average dark field scattering spectra of AgNPs, AgNPs@Cl, AgNPs@Br, AgNPs@I obtained experimentally (dotted lines) and fitted with a Lorentzian curve (solid line) [20]

In order to estimate the chemical interface damping, we have used Person's theory which provides a basis to quantify the plasmon dephasing rate due to electron transfer into surface energy states. [20] The plasmon dephasing rate, γ, is given by:

$$\gamma = \gamma_0 + C\frac{v_F}{r} \tag{7}$$

Where γ_0 is the bulk damping rate of silver, $\gamma_0 = 21\,meV$, v_F is the Fermi velocity, $v_F = 1.4\,nm/fs$, r is the radius of the nanoparticles, $r \approx 50\,nm$, and C is a factor which depends on the type of bond between the metal and the adsorbate. Therefore, C describes the rate of energy transfer from the plasmon resonance to adsorbate energy states. Considering the parameters above which were taken from Hartland et. al. [21], we can determine the C factor for each case based on the single particle dark field scattering measurements we took for AgNPs, AgNPs@Cl, AgNPs@Br, AgNPs@I which are presented in the following figure.

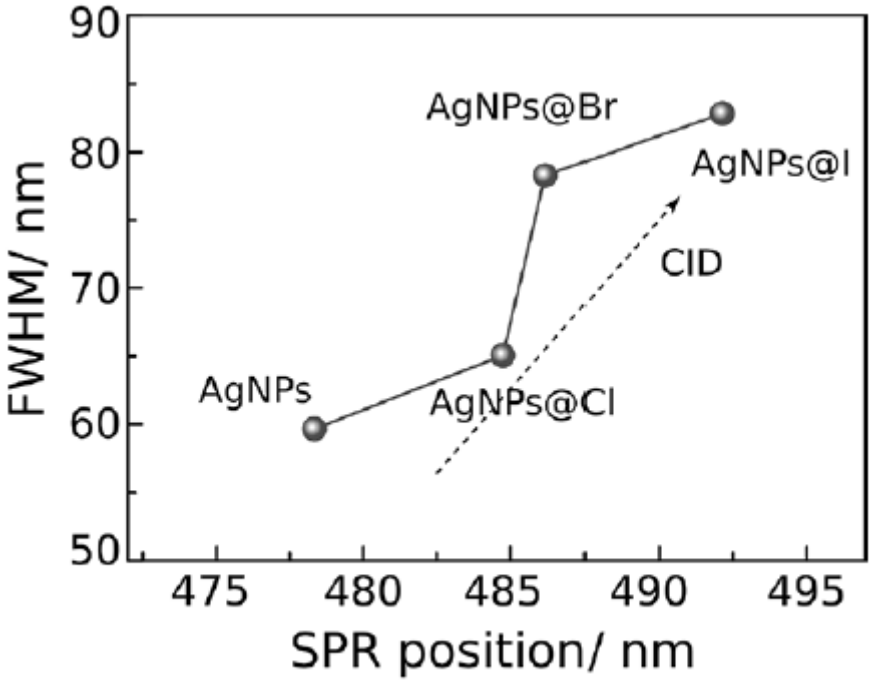

Figure 3.2 Averaged full-width at half-maximum (FWHM) and SPR position for AgNPs, AgNPs@Cl, AgNPs@Br, AgNPs@I showing an increase in the plasmon resonance decoherence after the sequential addition of the halide ions [20]

We have experimentally determined the average γ as the FWHM, for which we have calculated the C factor as presented in the following table.

Nanoparticle	C
AgNPs	0.75
AgNPs@Cl	0.82
AgNPs@Br	1.12
AgNPs@I	1.14

Table 3.1. The average C factor determined from single particle dark field scattering measurements [20]

From Table 4.1 we easily notice the increase in chemical interface damping and in the total decay rate is dependent on the chemical nature of the metal-molecule interface. We observe a higher increase in the CID of the plasmon resonance of AgNPs@Br and AgNPs@I compared to AgNPs@Cl.

To accommodate our experimental results, we hypothesized that hybrid, metal-halide energy states are formed due to halide-ion adsorption, which can, transiently, accept electrons, either from the plasmon resonance (increasing the decoherence of the SPR) or from excited molecules (increasing the non-radiative decay rate). The results presented in this study suggest that the addition of Br^- and I^- to AgNPs creates new metal-molecule hybrid energy states. [20]

3.2. CID at the interface of AgNPs due to CTP and BTP adsorption

After the successful analysis of the test system, we have gone further to investigate the correlation between chemical interface damping and the dehalogenation of CTP and BTP molecules.

First, we used the DFS set-up previously presented to analyze the interaction at a single particle level. After the AgNPs colloid has been dried inside a microfluidic cell, we pumped ethanol using the microfluidic pump and took a reference measurement, then we added a solution of 4-Bromotiophenol diluted in ethanol and left it to interact with the substrate for half an hour before taking a second measurement. The same procedure was applied for the 4-Clorotiophenol measurements.

Subsequently, the spectral images of 20 nanoparticles were taken for each case and analyzed using a Python script from which the full width at half maximum (FWHM) was

extracted. The same script was used to convert the FWHM to decay time and to extract the C factor, which quantifies chemical interface damping.

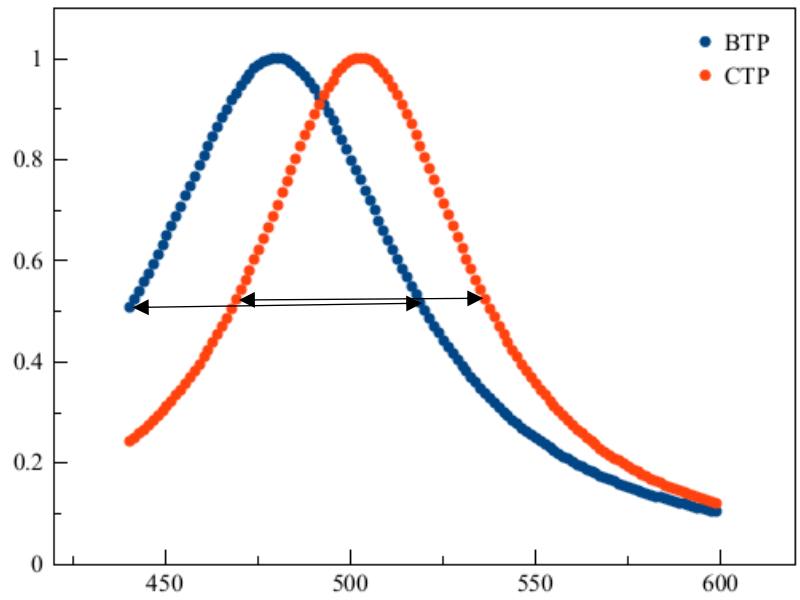

Figure 3.3 The average dark field scattering spectra fitted with a Lorentzian curve for BTP and CTP

It is noticeable that the FWHM for BTP is larger than that of CTP, which implies a larger damping rate and therefore a faster chemical reaction. Another noticeable aspect is the shift of the spectrum's maximum to the right, as can be seen in Figure 3.3.

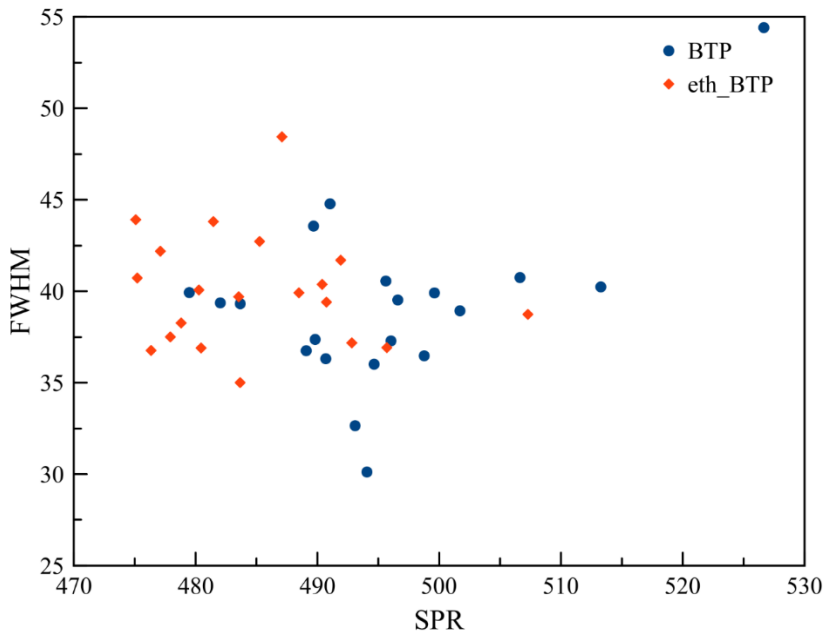

Figure 3.4. Linewidth vs. SPR wavelength for BTP

If we compare the spectra for AgNPs in ethanol with the spectra with added adsorbates, we notice the broadening of the LSPR linewidth, as well as a clear shift to the right (red shift), more prominent in the BTP measurements than in CTP ones, as shown in Figures 3.4 and 3.5. This confirms the previously reported fact that CID increases for more electronegative molecules, as Br^- has a higher electronegativity than Cl^-.

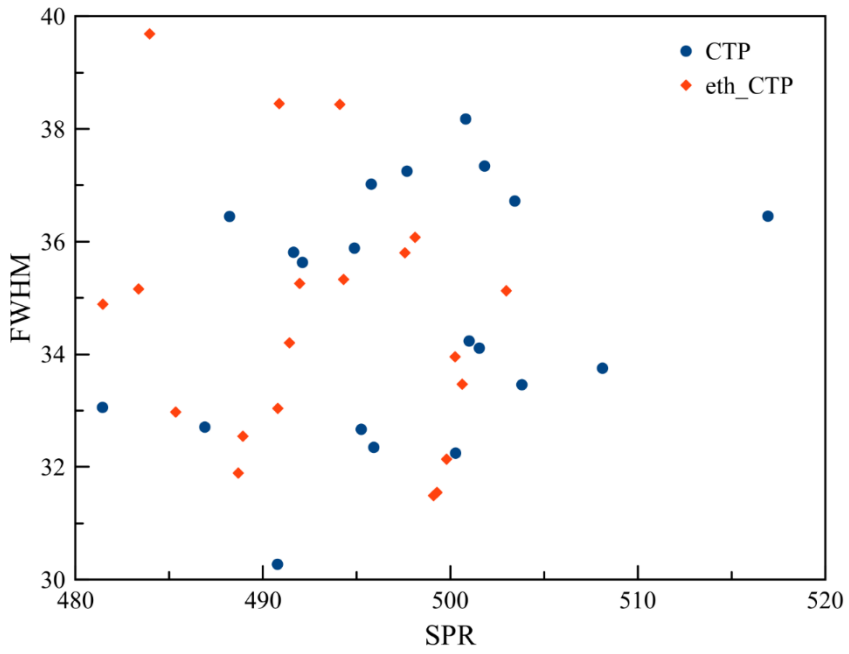

Figure 3.5. Linewidth vs. SPR wavelength for CTP

Finally, the C factor has been extracted from the measurements for each adsorbed molecule, resulting in the following table. We can attribute the difference between the two AgNPs@ethanol factors to lab conditions, but even so, the damping rate is obviously higher for BTP than for CTP, meaning a higher chemical interface damping.

Nanoparticle	C
AgNPs@ethanol	0.968
AgNPs@CTP	1.046
AgNPs@ethanol	1.209
AgNPs@BTP	1.230

Table 3.2 C factor determined from the experimental data

3.3. Dehalogenation of CTP and BTP tracked by SERS

After studying the chemical interface damping associated with each adsorbed molecule, we tracked the dehalogenation reaction through surface enhanced Raman scattering. We prepared a substrate as described in the second chapter, and then several 60 seconds time-series measurements were performed.

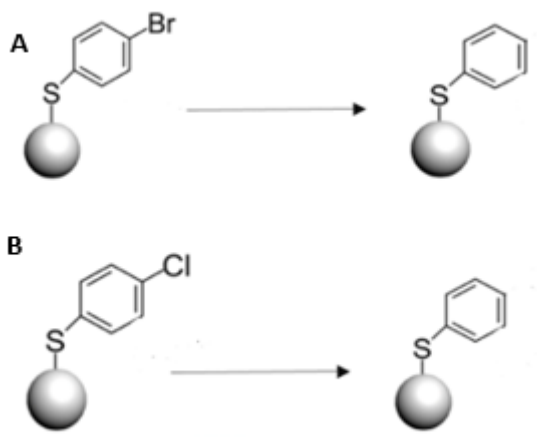

Figure 3.6. A. The dehalogenation reaction for BTP adsorbed on a silver substrate; B. The dehalogenation reaction for CTP adsorbed on a silver substrate

We tracked the C-Cl and C-Br vibrations bands, which correspond approximately to 1061 cm^{-1} and 1066 cm^{-1} respectively. We discovered a decrease in the intensity of these peaks which means the carbon-halogen bond is weakening and eventually breaking. The decrease in intensity in these vibration bands can be observed in the following two figures.

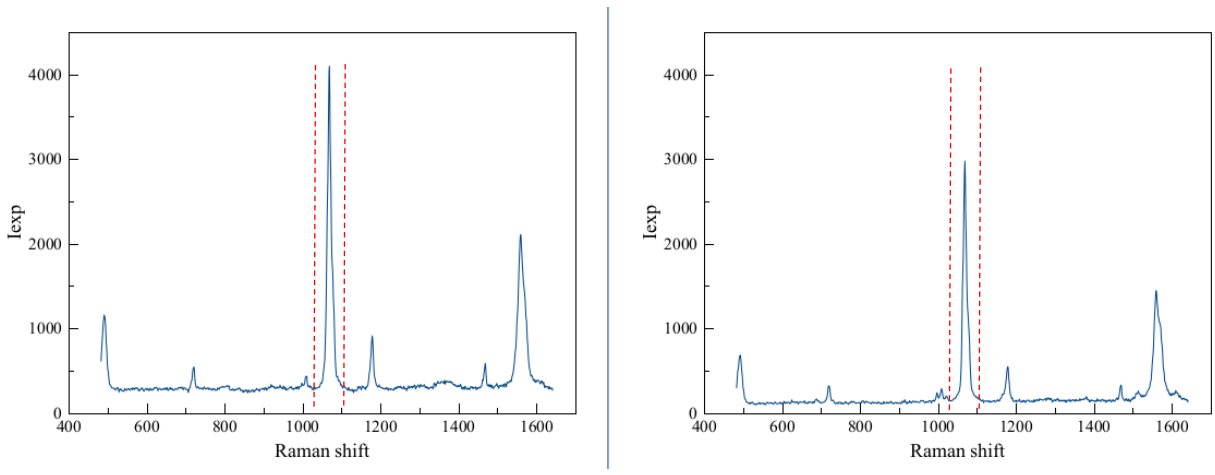

Figure 3.7. Left: SERS spectrum of AgNPs@BTP at t=0s; Right: SERS spectrum of AgNPs@BTP at t=60s; Marked with red: the peak corresponding to the C-Br bond

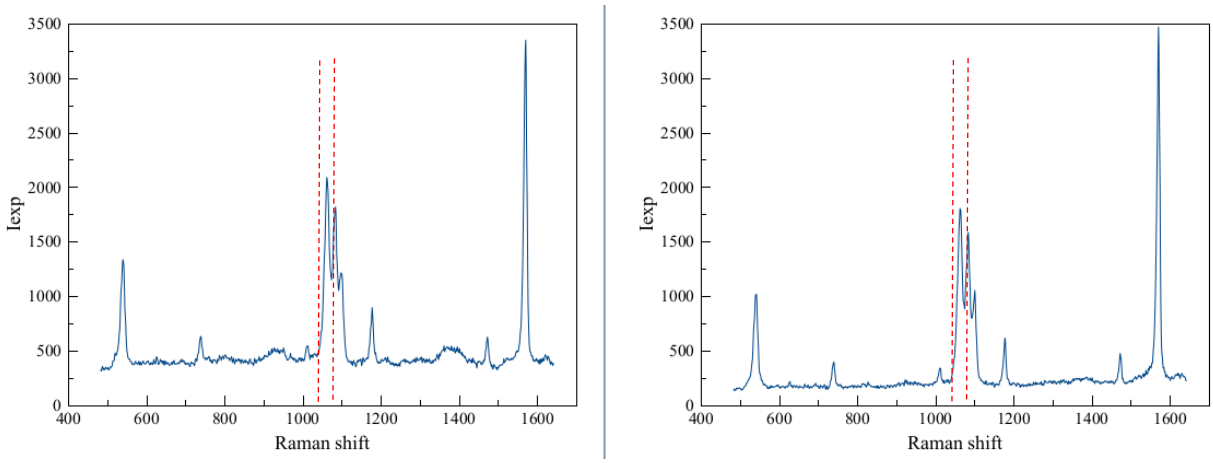

Figure 3.8. Left: SERS spectrum of AgNPs@CTP at t=0s; Right: SERS spectrum of AgNPs@CTP at t=60s; Marked with red: the peak corresponding to the C-Cl bond

After the peaks corresponding to the reaction were identified, a Matlab program was used to extract their intensities during the 60 s measurements. Then, using equation (1), the theoretical values were calculated, by giving k and h random values until the theoretical and experimental curves overlapped. Afterwards, using an Excel function to minimize the error between the theoretical and experimental values, the actual fractal reaction constant k was calculated.

Laser line	532 nm		633 nm	
Laser power	0.5%	1%	5%	10%
CTP	0.0036	0.0051	0.0012	0.0022
BTP	0.0054	0.0069	0.0032	0.0054

Table 3.3. The fractal reaction constant k for different laser lines and laser powers

By varying the reaction constant k, we observe that the dehalogenation reaction happens faster for BTP than for CTP, which correlated to the results provided by dark field scattering measurements, imply that an increase in chemical interface damping is responsible for the faster bond breaking.

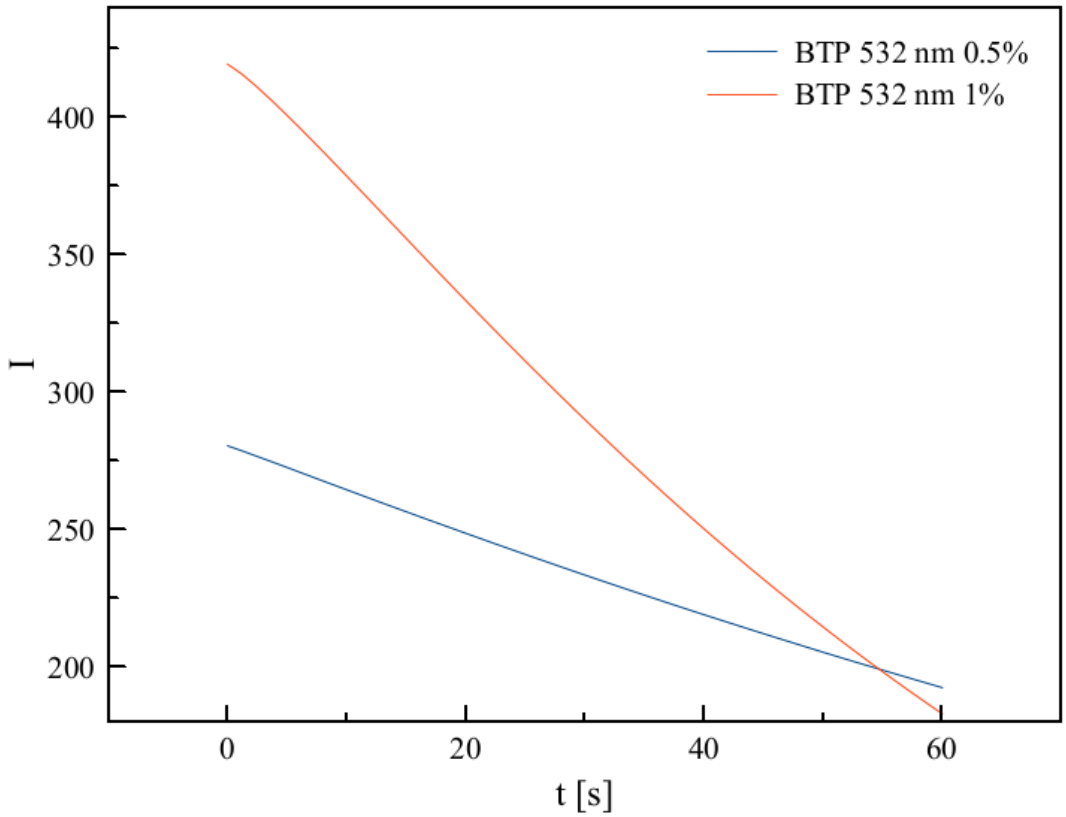

Figure 3.9. Graph showing the C-Br peak decreasing in intensity during laser illumination for the 532 nm laser line at 0.5% and 1% power

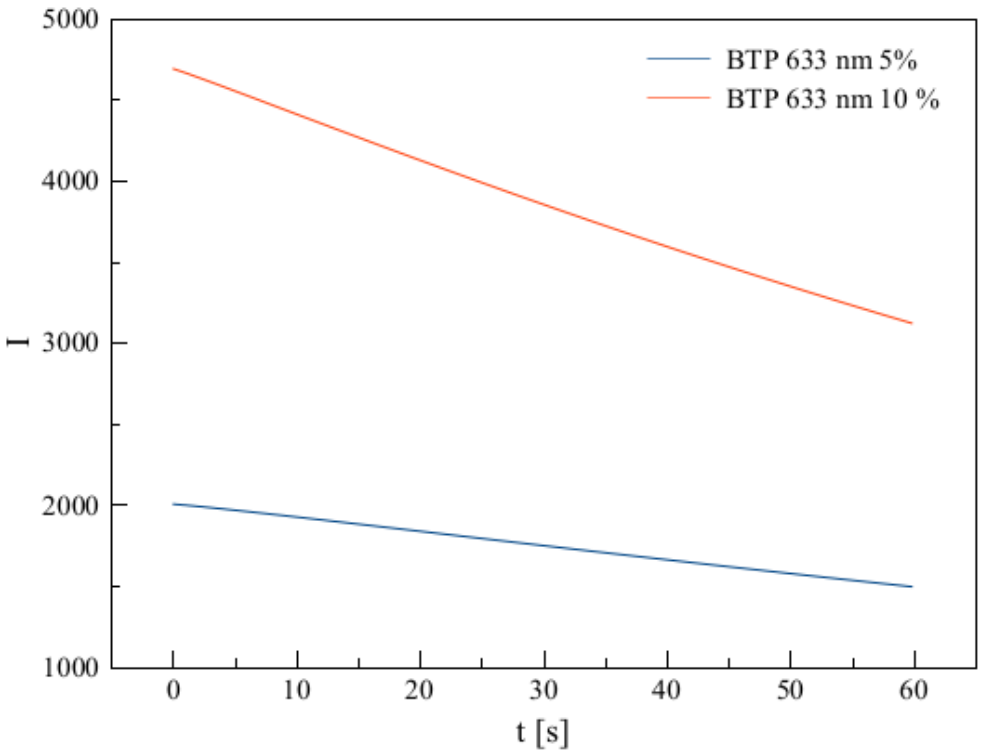

Figure 3.10. Graph showing the C-Br peak decreasing in intensity during laser illumination for the 633 nm laser line at 5% and 10% power

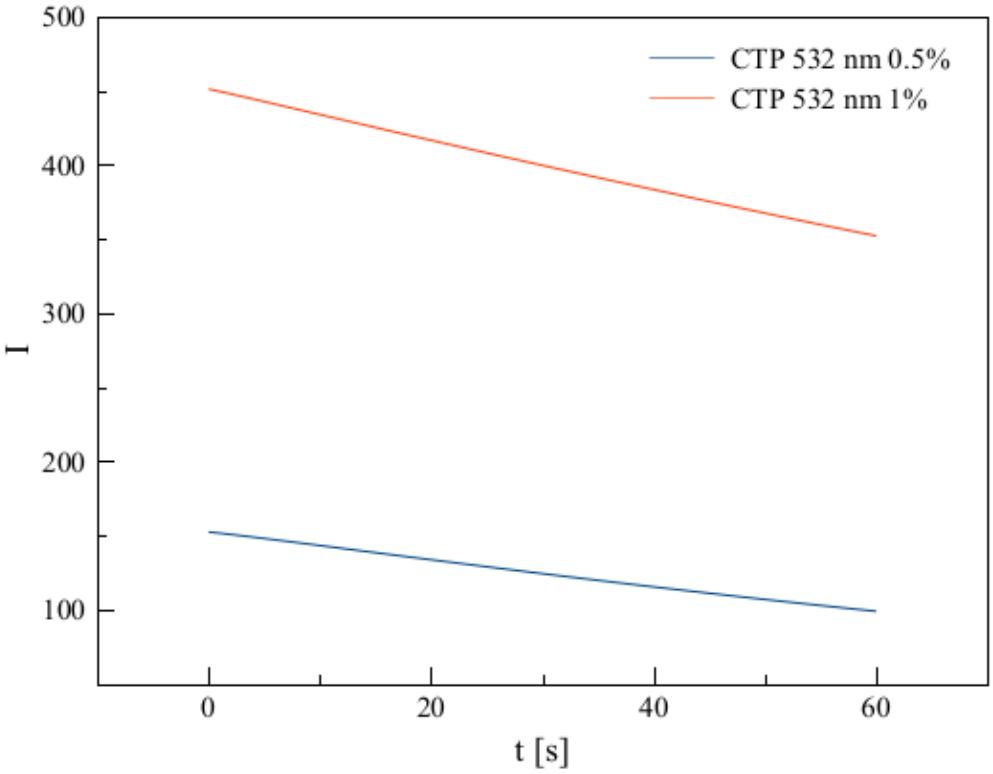

Figure 3.11. Graph showing the C-Cl peak decreasing in intensity during laser illumination for the 532 nm laser line at 0.5% and 1% power

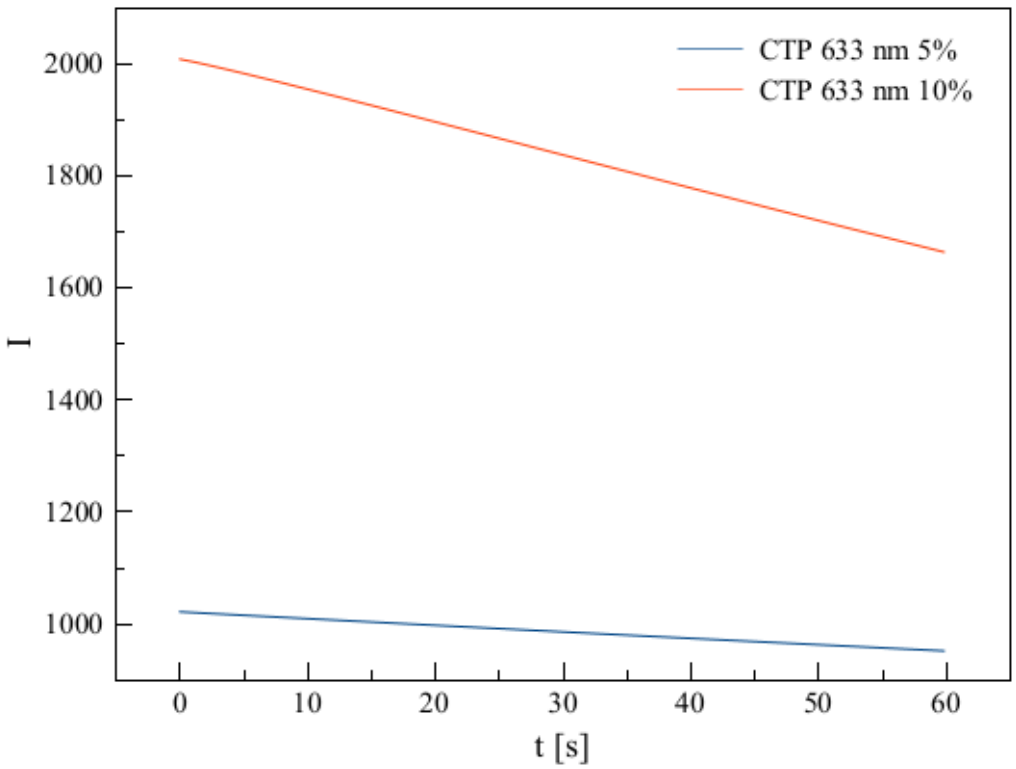

Figure 3.12. Graph showing the C-Cl peak decreasing in intensity during laser illumination for the 633 nm laser line at 5% and 10% power

Figures 3.9-3.12 offer comparisons between dehalogenation rates in relation to the laser power. We notice a high dependency of the reaction rate and the excitation laser which can be attributed to the fact that more electrons are generated under higher plasmonic activity.

Conclusions

This study presents the correlation between the chemical interface damping and the dehalogenation reaction rate by using surface enhanced Raman scattering and dark field scattering.

In order to quantify the chemical interface damping, we have performed several dark field scattering measurements at single particle level on 4-clorothiophenol (CTP) and 4-bromothiophenol (BTP) molecules adsorbed on silver nanoparticles. From the resulting spectra we have calculated the C factor which describes the rate of energy transfer from the plasmon resonance to the adsorbate.

The reaction rate constant has been calculated from several time-series acquired through surface enhanced Raman scattering measurements using different laser powers. From analyzing the measurements, we can observe that the dissociation rate of the thiol-halogen bond increases with the laser power, implying the creation of more hot carriers through plasmonic resonance, which when transferred to the adsorbate induce the bond breaking.

Finally, we corelate the chemical interface damping with the reaction rate by looking at constants C and k for CTP and BTP. We observe that the nanoparticles-adsorbate complex containing BTP has a higher rate of energy transfer than the one with CTP, C(BTP)>C(CTP) and at the same time, the reaction rate for BTP is higher than that of CTP, k(BTP)>k(CTP). Therefore, we can only conclude that the two are related and the higher the chemical interface damping, the higher the reaction rate.

The characterization of chemical interface damping induced bond breaking for carbon-halogen could prove a great potential for organic synthesis, especially the creation of CID-based biosensors.

Parts of this study have been published in ACS Photonics, in the following article: Andrei Stefancu, Oana M. Biro, Otto Todor-Boer, Ioan Botiz, Emiliano Cortes, Nicolae Leopold, Halide-Metal Complexes at Plasmonic Interfaces Create New Decay Pathways for Plasmons and Excited Molecules, ACS Photonics, 9 (3), 895-904, 2022.

References

[1] Cortes Emiliano, Activating plasmonic chemistry, Science, 362 (6410), 28-29, 2018

[2] Boerigter Calvin, Aslam Umar, Linic Suljo, Mechanism of Charge Transfer from Plasmonic Nanostructures to Chemically Attached Materials, ACS Nano, 10 (6), 6108-6115, 2016

[3] Stefancu Andrei, Iancu D. Stefania, Leopold F. Loredana, Leopold Nicolae, Contribution of chemical interface damping to the shift of surface plasmon resonance energy of gold nanoparticles, Romanian Reports in Physics, 72, 402, 1-12, 2020

[4] Cortes Emiliano, Besteiro V. Lucas, Alabastri Alessandro, Baldi Andrea, Tagliabue Giulia, Demetriadou Angela, Narang Prineha, Challenges in Plasmonic Catalysis, ACS Nano, 14 (12), 16202-16219, 2020

[5] Tigran V. Shahbazyan, Mark I. Stockman, Plasmonics: Theory and Applications, Springer, 2013, page 4

[6] Matthew Pelton, Garnett Bryant, Introduction to Metal-Nanoparticle Plasmonics, Wiley – Science Wise Publishing, 2013, pages 12-13

[7] P.C. Lee, D. Meisel, Adsorption and surface-enhanced Raman of dyes on silver and gold sols, J. Phys. Chem., 86, 2291-2295, 1982

[8] Jan Krajczewski, Karol Kolataj, Andrzej Kudelski, Plasmonic nanoparticles in chemical analysis, RSC Advances, 7, 17559-17576, 2017

[9] Calvin Boerigter, Umar Aslam, Suljo Linic, Mechanism of Charge Transfer from Plasmonic Nanostructures to Chemically Attached Materials, ACS Nano, 10, 6, 6108-6115, 2016

[10] Stephen A. Lee, Stephan Link, Chemical Interface Damping of Surface Plasmon Resonances, Accounts of Chemical Research, 54 (8), 1950-1960, 2021

[11] Seong Woo Moon, Ji Won Ha, Single Particle correlation study: chemical interface damping induced by biotinylated proteins with sulfur in plasmonic gold nanorods, Physical Chemistry Chemical Physics, 21, 7061-7066, 2019

[12] Eric C. Le Ru, Pablo G. Etchegoin, Principles of Surface-Enhanced Raman Spectroscopy and related plasmonic effects, Elsevier, 2009

[13] Song-Yuan Ding, En-Ming You, Zhong-Qun Tian and Martin Moskovits, Electromagnetic theories of surface-enhanced Raman spectroscopy, Chemical Society Reviews, 46, 4042-4076, 2017

[14] Milton Kerker, Dau-Sing Wang, H. Chew, Surface enhanced Raman scattering (SERS) by molecules adsorbed at spherical particles: errata, Applied Optics, 19, 4159-4174, 1980

[15] Ricardo Aroca, Surface-Enhanced Vibrational Spectroscopy, John Wiley and Sons, 2006

[16] Paula Zamora-Perez, Dionysia Tsoutsi, Ruixue Xu, Pilar Rivera_Gil, Hyperspectral-Enhanced Dark Field Microscopy for Single and Collective Nanoparticle Characterization in Biological Environments, Materials (Basel), 11 (2):243, 2018 Feb 6

[17] Min Hu, Carolina Novo, et al, Dark-field microscopy studies of single metal nanoparticles: understanding the factors that influence the linewidth of the localized surface plasmon resonance, J mater Chem., 18(17): 1949-1960, 2018

[18] Kedar Joshi, James F. Gilchrist, Estimation of drying length during particle assembly by convective deposition, Journal of Colloid and Interface Science 496, 222-227, 2017

[19] Cosmin Farcau, Neralagatta M. Sangeetha, Helena Moreira, Benoit Viallet, Jeremie Grisolia, Diana Ciuculescu-Pradines, Laurence Ressier, High-Sensitivity Strain Gauge Based on a Single Wire of Gold Nanoparticles Fabricated by Stop-and-Go Convective Self-Assembly

[20] Andrei Stefancu, Oana M. Biro, Otto Todor-Boer, Ioan Botiz, Emiliano Cortes, Nicolae Leopold, Halide-Metal Complexes at Plasmonic Interfaces Create New Decay Pathways for Plasmons and Excited Molecules, ACS Photonics, 9 (3), 895-904, 2022

[21] Hartland G. V., Besteiero L.V., Johns P., Govorov A. O., What's so hot about Electrons in Metal Nanoparticles?, ACS Energy Letters, 2 (7), 1641-1653, 2017

[22] Robin Schürmann, Alessandro Nagel, Sabrina Juergensen, Anisha Pathak, Stephanie Reich, Claudia Pacholski, and Ilko Bald, Microscopic Understanding of Reaction Rates Observed in Plasmon Chemistry of Nanoparticle–Ligand Systems, The Journal of Physical Chemistry C, 126 (11), 5333-5342, 2022

[23] Ping Jiang, Yueyue Dong, Ling Yang, Yaran Zhao, and Wei Xie, Hot Electron-Induced Carbon–Halogen Bond Cleavage Monitored by in Situ Surface-Enhanced Raman Spectroscopy, The Journal of Physical Chemistry C, 123 (27), 16741-16746, 2019

[24] Carsten Sönnichsen, Plasmons in metal nanostructures, Dissertation der Fakultät für Physik der Ludwig-Maximilians-Universität München, 2001